

# PROBABILITY FUSION FOR HYPERSPECTRAL AND LIDAR DATA

*Chiru Ge*

Shandong Normal University  
Information Science and Engineering  
Jinan 250358, China

*Qian Du\**

Mississippi State University  
Electrical and Computer Engineering  
Starkville, MS, 39762 USA

## ABSTRACT

In this paper, a new probability fusion strategy is proposed for hyperspectral and LiDAR data classification, which is inspired by the representation residual fusion strategy in our previous work. Unlike the residual fusion strategy utilizes a collaborative representation classifier, the probability fusion strategy deploys a deep residual network (DRN). This paper compares the two fusion strategies. The experiment results show that the probability fusion strategy with DRN is better than the residual fusion strategy in classification performance.

**Index Terms**— Hyperspectral image, LiDAR, residual fusion, classification, probability fusion

## 1. INTRODUCTION

Multi-source remote sensing images contain detailed information about the ground, e.g., LiDAR images with height and shape information and hyperspectral images (HSI) with spectral information. HSI and LiDAR images have complementary information. Therefore, fusion of the two data sources can further improve classification performance. However, automatic data fusion is still challenging.

HSI and LiDAR image fusion can be achieved by feature level fusion and decision level fusion. Many work of feature level fusion in the literature include the step of dimensionality reduction. Dimensionality reduction can be a feature selection problem. To utilize the entire datasets or all features, residual fusion is proposed under the framework of collaborative representation based classification [1], which belongs to decision level fusion. Inspired by residual fusion, a novel probability fusion method with deep residual network (DRN) [2] is proposed, which has the advantage of residual fusion and can achieve higher classification accuracy.

The main contributions of this paper are listed as follows.

- 1) This paper proposes a new method based on probability fusion for the fusion of HSI and LiDAR image.

- 2) The proposed probability fusion framework can be extended to any spatial features and any deep learning network structures for HSI and LiDAR data fusion.
- 3) The performance of residual fusion and probability fusion is fairly compared with the previous work on collaborative representation [1].

## 2. METHODOLOGY

Fig. 1 illustrates residual fusion for the classification of HSI and LiDAR images, which was proposed in [1]. In the residual fusion framework, spatial features of HSI and LiDAR are first extracted. Spatial features are the stacked features of extinction profile (EP) [3, 4], and local binary pattern (LBP) [5] due to their effectiveness. Then, the HSI spectral features, HSI spatial features, and LiDAR spatial features are normalized because different sources of data generally have different value ranges. After that, each source of data is input into a collaborative representation-based classifier with Tikhonov regularization (KCRT) classifier to obtain the residuals. Finally, the residuals are fused to acquire the reconstruction residual that can be used to finalize the class membership of a testing pixel.

Let  $r(y) = [r_1(y), r_2(y), \dots, r_l(y), \dots, r_C(y)]$  be the residual vector for a testing sample  $y$ , where  $C$  is the total number of classes. The equation of residual fusion can be expressed as

$$r(y) = abr_{HSI}(y) + b(1-a)r_{HSI\_EPLBP}(y) + (1-b)r_{LiDAR\_EPLBP}(y) \quad (1)$$

where  $a$  and  $b$  are the weighting parameters, and  $r_{HSI}(y)$ ,  $r_{HSI\_EPLBP}(y)$  and  $r_{LiDAR\_EPLBP}(y)$  denote the residual vectors from HSI spectral features, HSI spatial features, and LiDAR spatial features, respectively. The class label of  $y$  can be calculated by

$$\text{class}(y) = \arg \min_{l=1, \dots, C} (r(y)) \quad (2)$$

\*Thanks to the National Key R&D Program of China (2018YFB0505000).

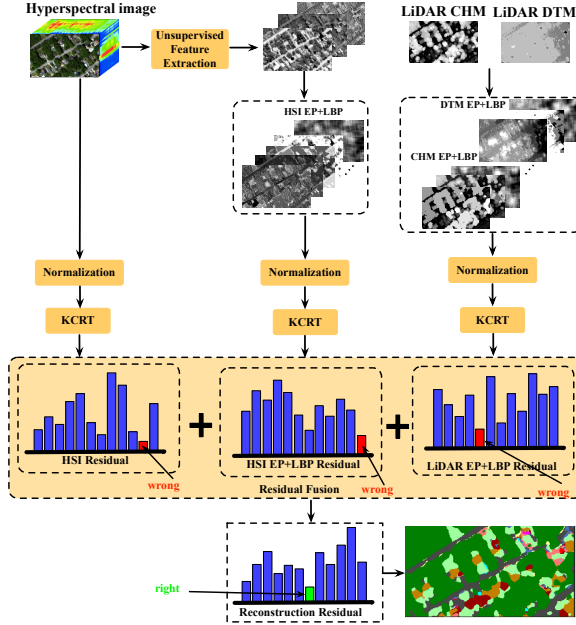


**Fig. 1.** Representation fusion for HSI and LiDAR data.

Fig. 1 shows a testing sample of the seventh class, which was misclassified by three classifiers utilizing every single source, but accurately classified by the representation residual fusion method.

Fig. 2 depicts our proposed probability fusion for HSI and LiDAR images, which was inspired by representation residual fusion. The difference is that probability fusion utilizes DRN to classify each source of data, and the testing pixel is assigned to the class with the largest fused probability. DRN acquires the probability matrices of each source. Finally, three probability matrices are fused to obtain the reconstruction probability that can be utilized to finalize the class label of a testing sample.

Let  $p(y) = [p_1(y), p_2(y), \dots, p_l(y), \dots, p_C(y)]$  be the probability vector for the testing sample  $y$ . The equation of probability fusion is expressed as

$$p(y) = cd p_{HSI}(y) + d(1 - c)p_{HSI\_EPLBP}(y) + (1 - d)p_{LiDAR\_EPLBP}(y) \quad (3)$$

where  $c$  and  $d$  are the weighting parameters, and  $p_{HSI}(y)$ ,  $p_{HSI\_EPLBP}(y)$  and  $p_{LiDAR\_EPLBP}(y)$  represent the probability vectors from HSI spectral features, HSI spatial features, and LiDAR spatial features, respectively. The class label of  $y$  can be computed by

$$\text{class}(y) = \arg \max_{l=1, \dots, C} (p(y)) \quad (4)$$

Fig. 2 also shows the testing sample of the seventh class, which was misclassified by three classifiers utilizing every

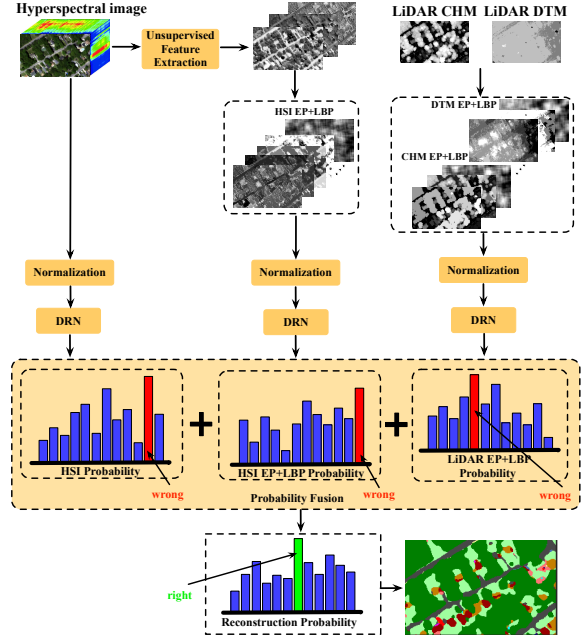


**Fig. 2.** Probability fusion for HSI and LiDAR data.

single source, but accurately classified by the probability fusion method.

The advantage of probability fusion and residual fusion is that they both can correct the wrong labels of single-source data. However, the two methods have two sensitive parameters to be tuned.

### 3. EXPERIMENTS

#### 3.1. Experiment data

Wertheim data come from Goddard's LiDAR, Hyperspectral, and Thermal (G-LiHT) data. The G-LiHT Airborne Imager [6] supplies co-registered LiDAR DTM, LiDAR CHM, LiDAR Point Cloud, hyperspectral reflectance image at 1m spatial resolution and google earth overlay by Keyhole Markup Language (KML) at 0.25m spatial resolution. The G-LiHT data can be downloaded for free<sup>1</sup>.

Experiments are conducted on the HSI, CHM, and DTM data which were collected in June 2016 across the Wertheim region (the geographical coordinate is at  $40^{\circ}46'30''$  latitude,  $-72^{\circ}52'48''$  longitude). The hyperspectral image has 114 bands with a spectral range of 420 nm to 950 nm. Spatial resolution of HSI, CHM, and DTM is 1 m. The data set of the entire scene contains  $501 \times 1523$  pixels. According to the calibration method [7], 15 categories are in the Wertheim data. Table 1 shows these categories and the corresponding number of training, validation, and testing samples. The validation set is used to control the training process of DRN. Fig.

<sup>1</sup><https://glihtdata.gsfc.nasa.gov>

3 gives HSI, CHM, DTM, the labeled ground-truth, positions of training samples, positions of validation samples, positions of testing samples, and legend of 15 categories.

**Table 1.** Wertheim: number of training, validation and testing samples

No	Name	Number of samples		
		Training	Validation	Testing
1	Tree	811	969	177163
2	Sea	182	224	10416
3	Sand	130	135	4548
4	Commercial	96	95	1024
5	Pool/Water	50	44	191
6	Major thoroughfares	334	382	4604
7	Bare soil	326	328	6230
8	Road	372	370	6893
9	Parking lot	191	163	1458
10	Grass	296	303	2890
11	Residential grey	116	119	725
12	Residential coffee	144	144	1271
13	Solar panel	30	30	95
14	Car	116	113	420
15	Electric wire	138	140	1052
Total		3332	3559	218980

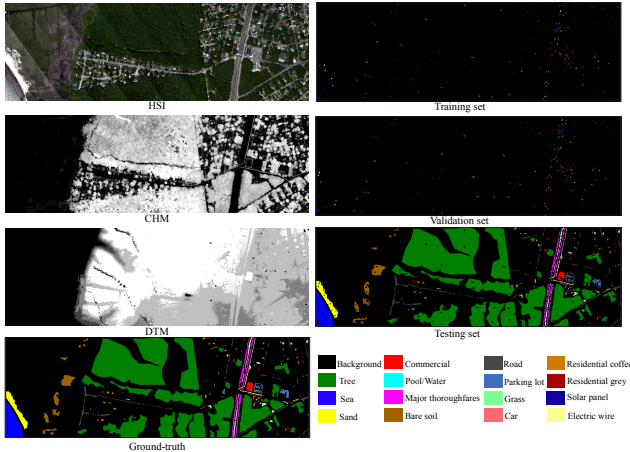


**Fig. 3.** Wertheim—the HSI data utilizing bands 20, 30 and 40, as blue, green and red respectively; LiDAR CHM image; LiDAR DTM image; Ground-truth; labeled training samples; labeled validation samples; labeled testing samples; the legend of different classes.

### 3.2. Parameter setting

Appropriate parameters of KCRT and DRN need to be set. But, due to the limited space, the detailed parameter tuning process of KCRT and DRN is not shown.

Fig. 4 shows the parameter tuning process for residual fusion and probability fusion. For residual fusion parameters

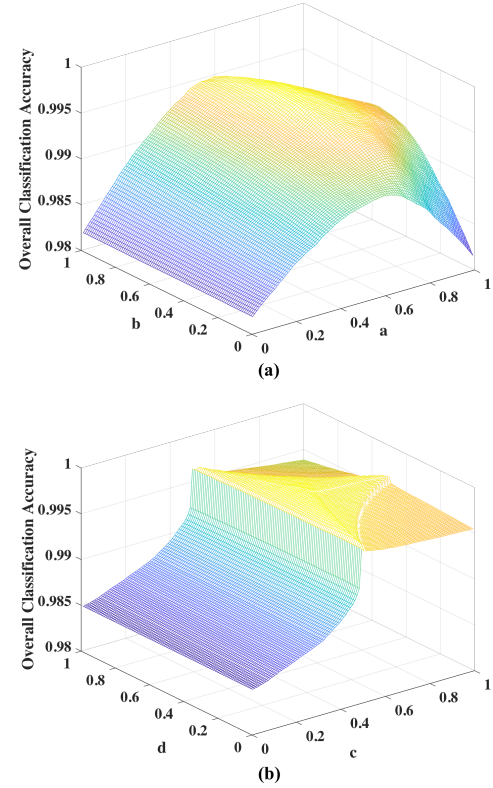


**Fig. 4.** Fusion parameters tuning process: (a) residual fusion; (b) probability fusion.

*a* and *b*, the optimal parameter are selected through Fig. 4 (a): *a* is 0.71 and *b* is 0.66. For probability fusion, the best parameters *c* and *d* are 0.48 and 0.62, respectively.

In the experiments, common classification metrics, i.e., AA, OA, Kappa are utilized.

### 3.3. Result and discussion

Table 2 shows classification results of residual fusion. As shown in Table 2, residual fusion offers higher classification accuracy than using each individual source, which illustrates the validity of residual fusion.

Table 3 shows classification results of our proposed probability fusion. As shown in Table 3, classification accuracy of probability fusion is higher than that of each source, which illustrates the validity of probability fusion. Compared with Table 2, classification accuracy of probability fusion is higher than that of residual fusion. The reason is that the classification performance of DRN is superior to KCRT.

Table 4 shows improved classification accuracy by residual fusion and probability fusion, compared with the corresponding counterpart using all the sources. Table 4 presents that residual fusion improves classification accuracy more than probability fusion, which demonstrates the potential of residual fusion.

**Table 2.** Classification results of residual fusion

	HSI KCRT	HSI_EPLBP KCRT	LiDAR_EPLBP KCRT	Residual Fusion
1	99.92	99.20	99.57	99.99
2	92.59	99.89	99.81	100.00
3	100.00	100.00	98.46	100.00
4	49.80	51.07	100.00	92.29
5	97.38	100.00	96.34	100.00
6	92.72	91.09	85.25	98.00
7	100.00	100.00	99.86	100.00
8	89.57	86.28	79.92	96.27
9	81.07	73.73	76.27	79.63
10	99.24	93.98	73.94	98.51
11	77.38	99.45	98.76	99.59
12	99.61	100.00	99.61	100.00
13	65.26	100.00	100.00	100.00
14	72.62	97.62	98.81	99.05
15	61.03	74.14	99.90	89.07
OA	98.40	98.11	98.15	99.58
AA	85.21	91.10	93.77	96.83
Kappa	0.9530	0.9453	0.9462	0.9877

**Table 3.** Classification results of probability fusion

	HSI DRN	HSI_EPLBP DRN	LiDAR_EPLBP DRN	Probability Fusion
1	100.00	100.00	100.00	100.00
2	100.00	100.00	98.98	100.00
3	99.98	100.00	95.13	100.00
4	98.51	100.00	100.00	78.42
5	100.00	99.48	97.95	100.00
6	92.90	99.06	84.03	99.52
7	100.00	100.00	99.48	100.00
8	97.39	94.53	96.81	98.94
9	84.25	83.26	93.06	94.31
10	97.04	94.66	71.27	99.79
11	100.00	100.00	100.00	99.31
12	100.00	99.61	84.01	100.00
13	95.00	96.94	100.00	100.00
14	85.28	83.72	41.47	97.62
15	69.21	94.98	79.86	90.11
OA	99.39	99.54	98.48	99.76
AA	94.64	96.42	89.47	97.20
Kappa	0.9820	0.9865	0.9553	0.9929

To summarize, residual fusion and probability fusion are both useful for HSI and LiDAR data fusion classification. Although probability fusion with DRN is better than residual fusion with KCRT in performance, residual fusion combined with a better representation classifier may further improve performance.

#### 4. CONCLUSIONS

A new probability fusion strategy is proposed for HSI and LiDAR data fusion. Our proposed probability fusion framework can be extended to any spatial features and any deep learning network structures for HSI and LiDAR data fusion. The experimental results show that the DRN-based probability fusion outperforms the KCRT-based representation residual fusion.

#### 5. ACKNOWLEDGMENT

The authors would like to thank NASA for the Wertheim data.

**Table 4.** Improvement of classification accuracy by residual fusion and probability fusion

		HSI	HSI_EPLBP	LiDAR_EPLBP
Residual Fusion-KCRT	OA	+1.18	+1.47	+1.43
	AA	+11.62	+5.73	+3.06
	Kappa	+0.0347	+0.0424	+0.0415
Probability Fusion-DRN	OA	+0.37	+0.22	+1.28
	AA	+2.56	+0.78	+7.73
	Kappa	+0.109	+0.0064	+0.0376

## 6. REFERENCES

- [1] C. Ge, Q. Du, W. Li, Y. Li, and W. Sun, “Hyperspectral and lidar data classification using kernel collaborative representation based residual fusion,” *IEEE Journal of Selected Topics in Applied Earth Observations and Remote Sensing*, pp. 1–11, 2019.
- [2] Z. Zhong, J. Li, Z. Luo, and M. Chapman, “Spectral-spatial residual network for hyperspectral image classification: A 3-d deep learning framework,” *IEEE Transactions on Geoscience and Remote Sensing*, vol. 56, no. 2, pp. 847–858, 2018.
- [3] P. Ghamisi, R. Souza, J. A. Benediktsson, X. X. Zhu, L. Rittner, and R. A. Lotufo, “Extinction profiles for the classification of remote sensing data,” *IEEE Transactions on Geoscience and Remote Sensing*, vol. 54, no. 10, pp. 5631–5645, 2016.
- [4] P. Ghamisi, R. Souza, J. A. Benediktsson, L. Rittner, R. Lotufo, and X. X. Zhu, “Hyperspectral data classification using extended extinction profiles,” *IEEE Geoscience and Remote Sensing Letters*, vol. 13, no. 11, pp. 1641–1645, 2016.
- [5] W. Li, C. Chen, H. Su, and Q. Du, “Local binary patterns and extreme learning machine for hyperspectral imagery classification,” *IEEE Transactions on Geoscience and Remote Sensing*, vol. 53, no. 7, pp. 3681–3693, 2015.
- [6] Bruce Cook, Lawrence Corp, Ross Nelson, Elizabeth Middleton, Douglas Morton, Joel McCorkel, Jeffrey Masek, Kenneth Ranson, Vuong Ly, and Paul Montesano, “Nasa goddard’s lidar, hyperspectral and thermal (g-liht) airborne imager,” *Remote Sensing*, vol. 5, no. 8, pp. 4045, 2013.
- [7] Yunsong Li, Chiru Ge, Weiwei Sun, Jiangtao Peng, Qian Du, and Keyan Wang, “Hyperspectral and lidar data fusion classification using superpixel segmentation-based local pixel neighborhood preserving embedding,” *Remote Sensing*, vol. 11, no. 5, 2019.